Supporting Information

Oxygen vacancy-dependent photocatalytic activity of well-defined $Bi_2Sn_2O_{7-x}$ hollow nanocubes for NO_x removal

Yanfeng Lu[a,b], Meijuan Chen[c], Tingting Huang[a], Yu Huang[a,b,], Jun-ji Cao[a,b], Haiwei Li[d], Wingkei Ho,[e] and Shun Cheng Lee[d]*

[a.]Key Laboratory of Aerosol Chemistry and Physics, State Key Lab of Loess and Quaternary Geology (SKLLQG), Institute of Earth Environment, Chinese Academy of Sciences, Xi'an 710061, China

[b.]CAS Center for Excellence in Quaternary Science and Global Change, Institute of Earth Environment, Chinese Academy of Sciences, Xi'an 710061, China

[c.]School of Human Settlements and Civil Engineering, Xi'an Jiaotong University, Xi'an 710049, China

[d.]Department of Civil and Environmental Engineering, The Hong Kong Polytechnic University, Hung Hom, Hong Kong, China

[e.]Department of Science and Environmental Studies, The Hong Kong Institute of Education, Hong Kong, China

*Corresponding author: Prof. Yu Huang

E-mail address: huangyu@ieecas.cn

Tel: +86-02962336261

Supporting Information consists of 13 pages containing 5 method descriptions, 2 tables and 13 figures.

CONTENTS

Method S1. Synthesis of $Bi_2Sn_2O_7$ hollow nanocubes.

$BiC_6H_5O_7$ (3 mmol) was first added to 35 mL of NaOH solution (1.0 mol·L^{-1}) and then treated by ultrasonic wave for 30 minutes. $K_2SnO_3·3H_2O$ (3 mmol) was dissolved in a Teflon liner with 100 mL capacity containing 35 mL NaOH solution (1.0 mol·L^{-1}) and stirred for a short time. The mixed precipitates were formed by adding $BiC_6H_5O_7$ suspension to the Sn precursor solution dropwise. The Teflon liner was sealed in the stainless steel autoclave and kept at 180 °C for 24 h. The resulting yellowish powder was collected by washing several times with deionized water and drying at 80 °C.

Method S2. Photoelectrochemical analysis.

The photoelectrochemical properties of pristine $Bi_2Sn_2O_7$ and oxygen-vacancy $Bi_2Sn_2O_{7-x}$ hollow nanocubes were evaluated using a electrochemical workstation (Parstat4000, USA) in a conventional three-electrode cell with a platinum plate and an Ag/AgCl electrode as the counter and reference electrodes, respectively. The photocurrent-time curves were recorded at 0.2 V vs. Ag/AgCl in 0.5 mol·L^{-1} Na_2SO_3 at ambient temperature under irradiation with a 100 W LED lamp (λ = 420 nm). Electrochemical impedance spectroscopy (EIS) was conducted under open-circuit voltage in 1 mmol·L^{-1} $K_3Fe(CN)_6$ and $K_4Fe(CN)_6$ solution.

Method S3. Temperature programmed desorption (TPD) analysis.

The TPD experiments were performed on a chemisorption analyzer (BJbuilder, PCA 1200, China) equipped with a thermal conductivity detector (TCD). O_2–TPD and NO–TPD was performed with 0.5 g and 0.2 g samples using He gas as the carrier gas. The pretreatment of raw sample is firstly applied in pure He with a flow rate of 40 mL·min^{-1} at 120 °C for 180 min. After the pretreatment sample cooled down to room temperature, O_2–TPD measurement

was performed up to 800 °C at a heating rate of 7 °C·min^{-1} in He atmosphere with a flow rate of 25 mL·min^{-1}. The NO–TPD experiments were dosed with 50 ppm NO for 30 min to reach the absorption equilibrium after pretreated with pure He. Then the catalysts were purged with pure He gas with a flow rate of 25 mL·min^{-1} for 90 min to remove gas-phase NO completely. Finally, NO–TPD was performed up to 800 °C at a heating rate of 7 °C·min^{-1} in He atmosphere with a flow rate of 25 mL·min^{-1}.

Method S4. Photocatalytic activity analysis.

The photocatalytic activity of as-prepared catalysts were evaluated in a continuous-flow chamber with a 4.5 L capacity (30 cm × 15 cm × 10 cm), which was similar to that in the ISO 22197-1 standard. The removal efficiency of NO was evaluated by 0.2 g of samples pread on a quartz dish placed at the center of the reactor. The initial NO concentrations was 400 ppb for visible light radiation, supplied by a 300 W Xenon lamp through a 420 nm cutoff filter (Perfect Light MICROSOLAR 300, China). After the adsorption-desorption equilibrium by injecting the 400 ppb NO at a volume rate of 3 L·min^{-1} for at least 30 min, the visible light was turned on and the concentration of NO and NO_2 was continuously measured by a chemiluminescence NO*x* analyzer (Ecotech 9841, Australia). The removal efficiency of NO at any given time was denoted as C/C_o, where C_o is the initial concentration and of NO, ppb. NO_2 concentration was simultaneously recorded during photocatalytic reaction.

Method S5. Density Functional Theory (DFT) Calculations.

All DFT calculations are performed using the Cambridge Serial Total Energy Package (CASTEP), in which the electron-ion interactions are expressed by ultrasoft pseudo potentials, and the generalized gradient approximation (GGA) proposed by Perdew–Burke–Ernzerhof

(PBE) is used to describe the exchange-correlation energies and potential. The cutoff energy is set as 400 eV. The structure relaxation was performed until the convergence criteria of energy and force reached 2×10^{-5} eV and 0.05 eV/Å, respectively. The Brillouin zone is sampled by a 3×3×3 k-points grid generated via the Monkhorst-Pack procedure. We first optimized the $Bi_2Sn_2O_7$ unit cell, and calculate the band gap, the results show that the lattice parameter is a = 10.78 Å, which is close to the experimental results (10.87 Å). Meanwhile, the calculated band gap is estimated 2.73 eV. The comparison between the perfect and O vacancy $Bi_2Sn_2O_7$ were then calculated from the resulting calculation values.

Table S1. Oxygen vacancy formation energies (eV) on the surfaces of $Bi_2Sn_2O_7$.

Oxygen vacancy	E_{ads} (eV)
V_{O1} (Sn-adjacent)	3.15
V_{O2} (Bi-adjacent)	3.67

Table S2. Key structure parameters and adsorption energies of the stable configurations for the adsorbed species NO on different defect surfaces.

Surface	E_{ads} (eV)	Adsorption configuration	D_{NO-X} (Å)	Bonding details	
				bond	length (Å)
$Bi_2Sn_2O_7$	-2.67	top: via N	1.37	N-O	1.23
V_{O1}-$Bi_2Sn_2O_{7-x}$(Sn-adjacent)	-2.84	top: via N	1.32	N-O	1.25
V_{O2}-$Bi_2Sn_2O_{7-x}$(Bi-adjacent)	-1.67	hollow: via N	1.89/2.71/2.92	N-O	1.25

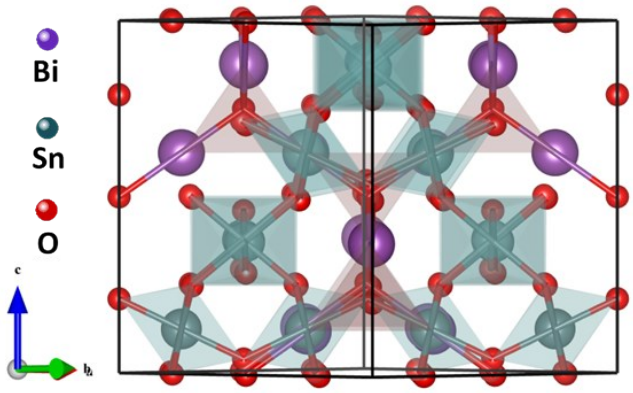

Figure S1. Schematic crystal structures of $Bi_2Sn_2O_7$. Color codes: Bi: purple, Sn: teal, O: red. Shading regions: pink, tetrahedron; gray, octahedron.

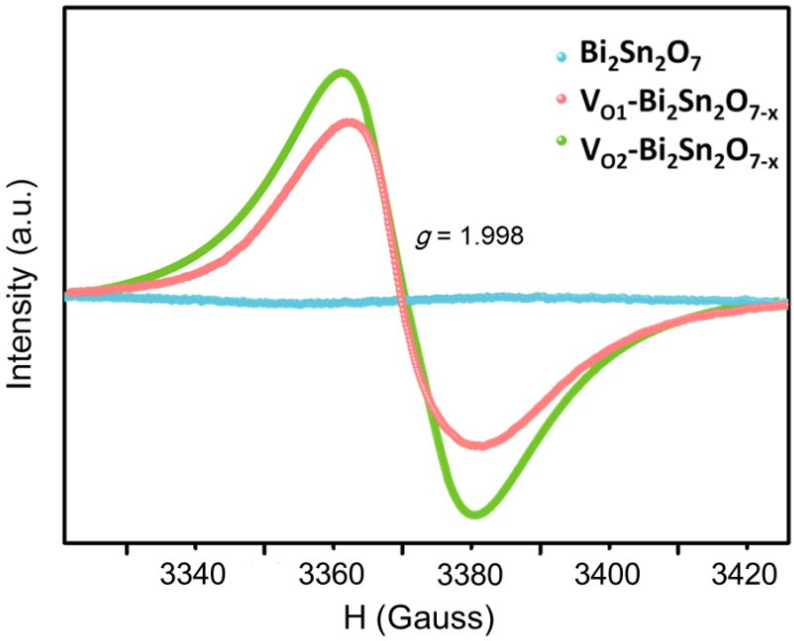

Figure S2. EPR spectra of pristine $Bi_2Sn_2O_7$ and $Bi_2Sn_2O_{7-x}$ samples.

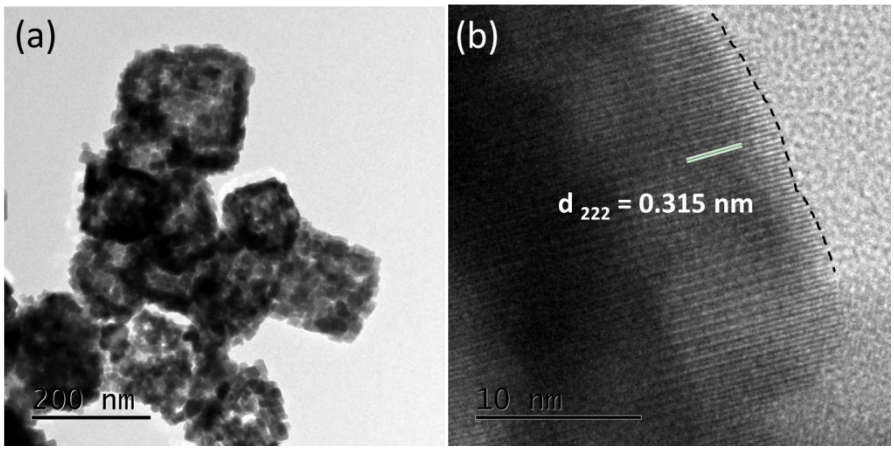

Figure S3. (a) TEM and (b) HR-TEM images of $Bi_2Sn_2O_7$.

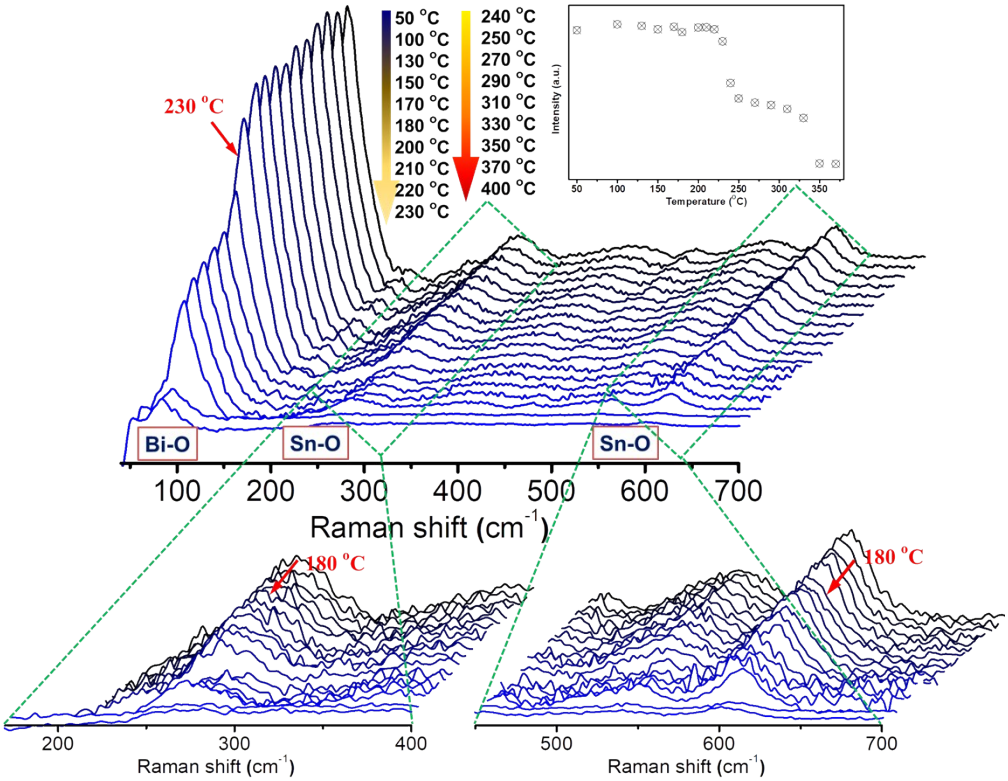

Figure S4. *In situ* Raman spectrum of pristine $Bi_2Sn_2O_7$ sample in the range from 50 to 400 °C, the inset shows the ball-and-stick model of $Bi_2Sn_2O_7$ coordination and the formation of oxygen vacancies in different spatial location (inset represents the peak intensity of stretching modes from the Bi-O bonds in $Bi_2Sn_2O_7$).

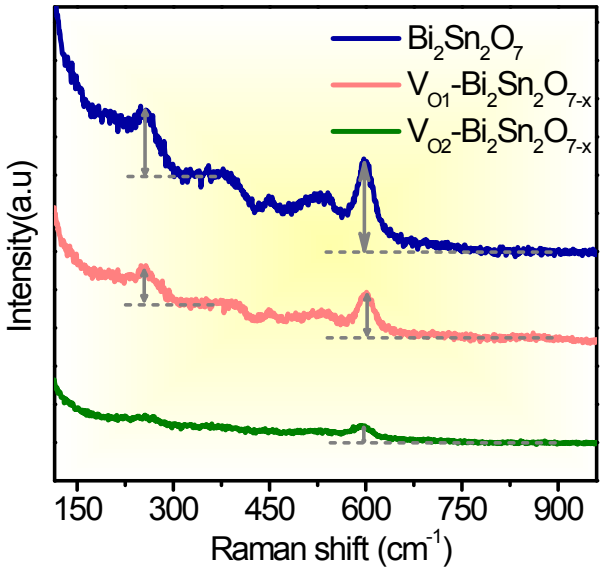

Figure S5. Raman spectrum of pristine $Bi_2Sn_2O_7$, V_{O1}-$Bi_2Sn_2O_{7-x}$ and V_{O2}-$Bi_2Sn_2O_{7-x}$ samples.

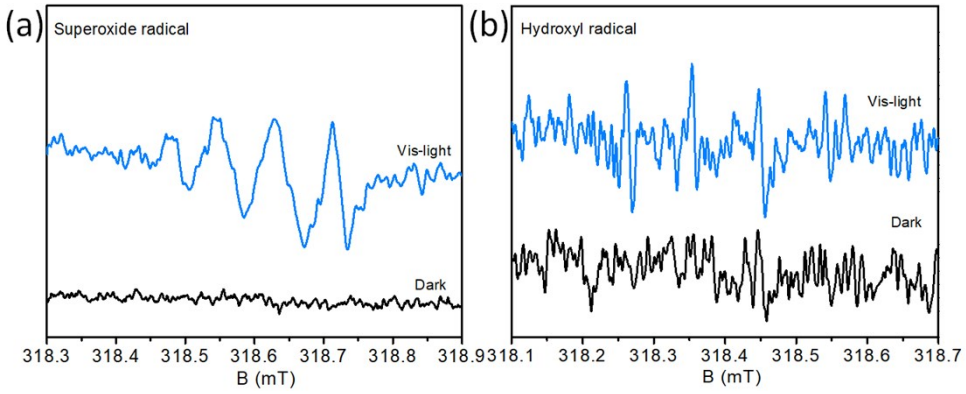

Figure S6. Generation of $\bullet O_2^-$ (a) and •OH (b) over V_{O2}-$Bi_2Sn_2O_{7-x}$.

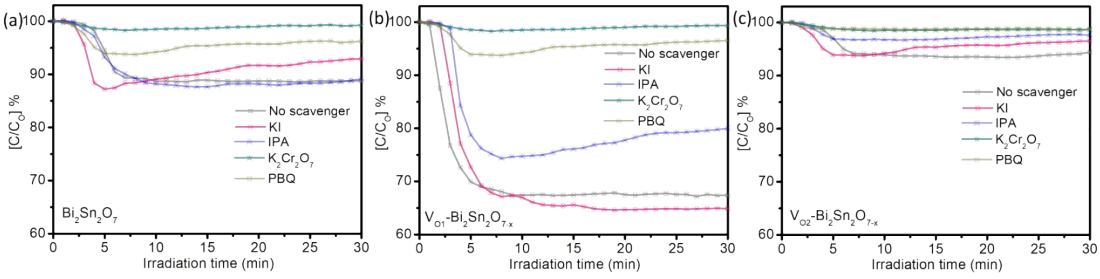

Figure S7. Active species trapping for NO removal over (a) $Bi_2Sn_2O_7$, (b) V_{O1}-$Bi_2Sn_2O_{7-x}$ (c)

V_{O2}-$Bi_2Sn_2O_{7-x}$ with different scavengers (KI →h^+; IPA →•OH; $K_2Cr_2O_7$ → e^-; PBQ →•O_2^-).

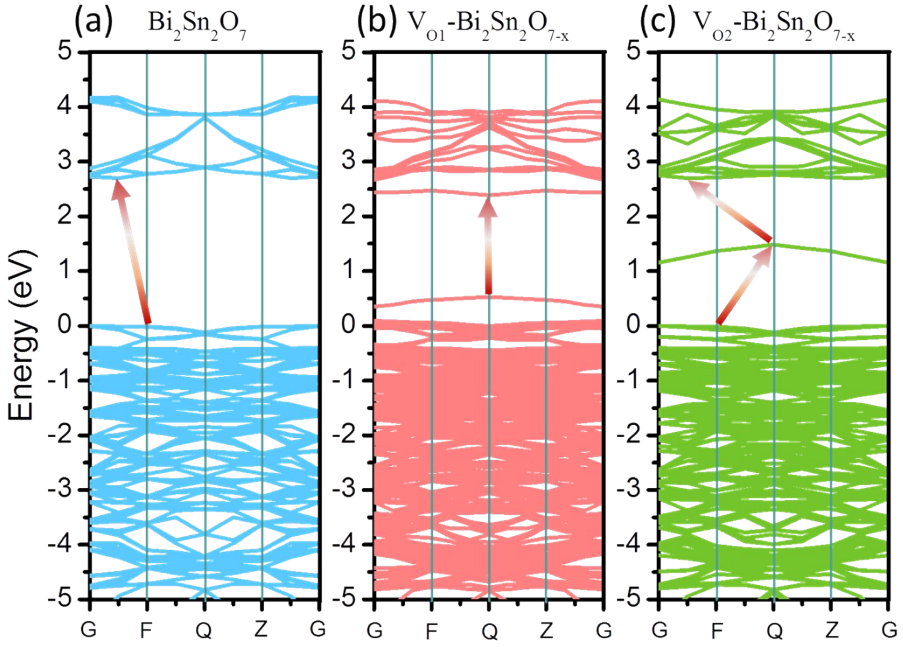

Figure S8. The band structure for $Bi_2Sn_2O_7$, V_{O1}-$Bi_2Sn_2O_{7-x}$(Sn–adjacent) and V_{O2}-$Bi_2Sn_2O_{7-x}$(Bi-adjacent), respectively.

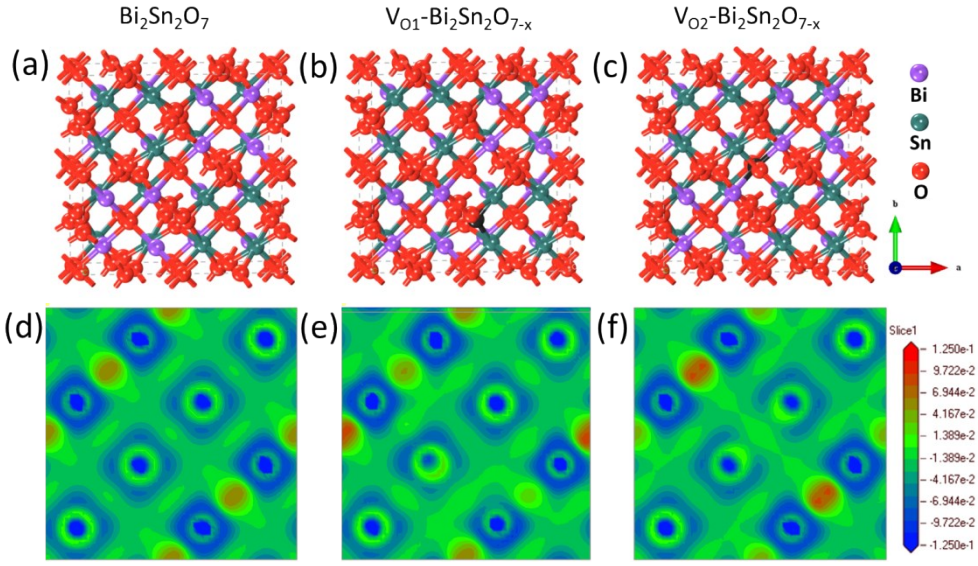

Figure S9. Electron density difference of $Bi_2Sn_2O_7$, V_{O1}-$Bi_2Sn_2O_{7-x}$(Sn-adjacent) and V_{O2}-$Bi_2Sn_2O_{7-x}$(Bi-adjacent) samples.

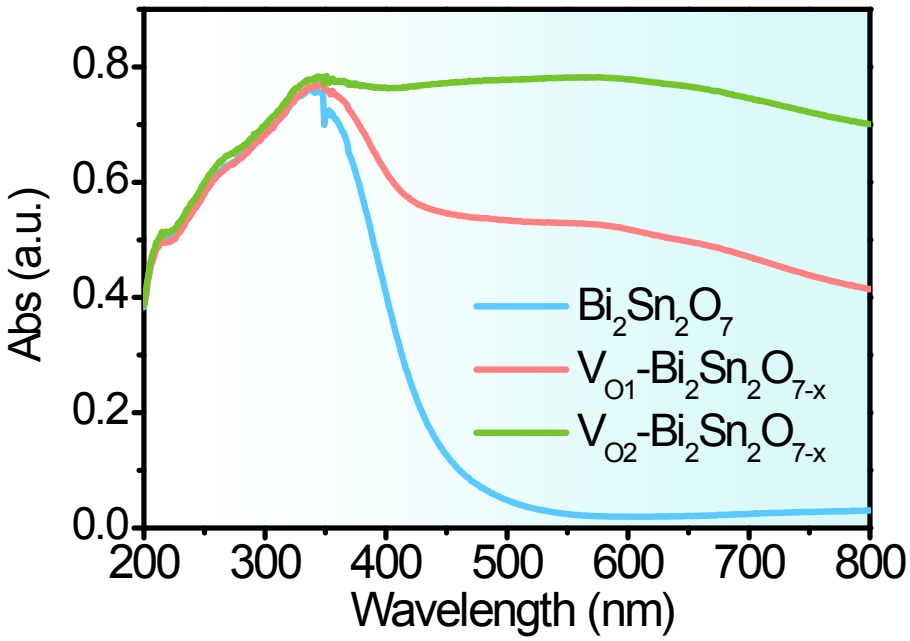

Figure S10. UV-vis DRS spectra of $Bi_2Sn_2O_7$, V_{O1}-$Bi_2Sn_2O_{7-x}$ and V_{O2}-$Bi_2Sn_2O_{7-x}$.

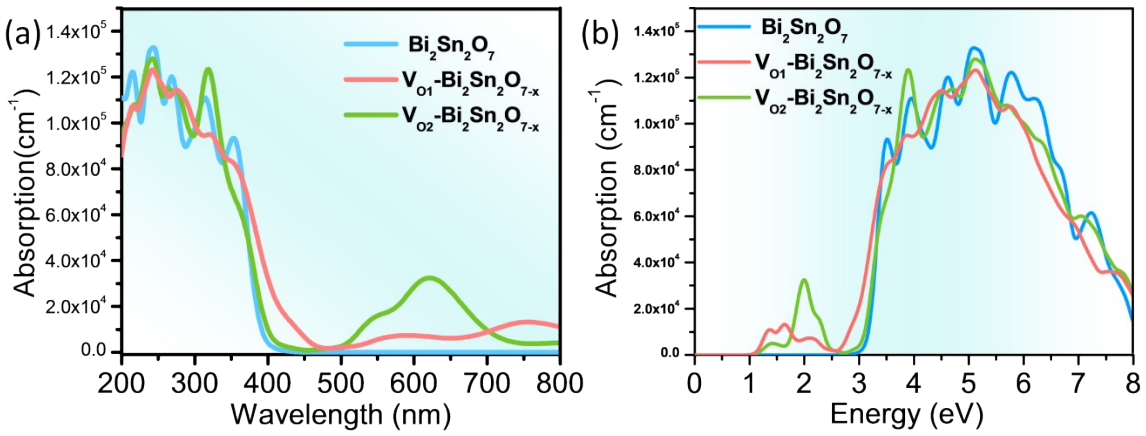

Figure S11. The absorption spectra of $Bi_2Sn_2O_7$, V_{O1}-$Bi_2Sn_2O_{7-x}$(Sn-adjacent) and V_{O2}-$Bi_2Sn_2O_{7-x}$(Bi-adjacent) as functions of (a) wavelength and (b) energy a using DFT method.

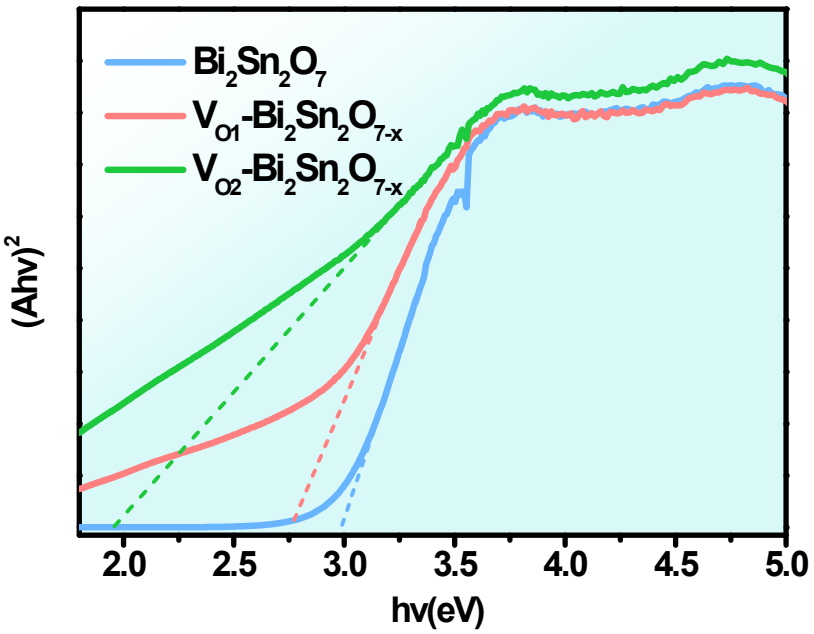

Figure S12. $(Ahν)^2$ vs hν of pristine $Bi_2Sn_2O_7$, V_{O1}-$Bi_2Sn_2O_{7-x}$ and V_{O2}-$Bi_2Sn_2O_{7-x}$ samples.

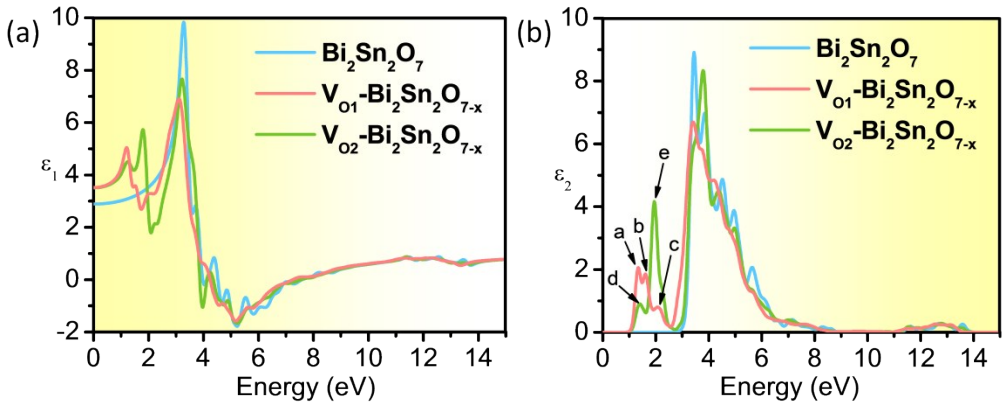

Figure S13. Dielectric Function of $Bi_2Sn_2O_7$, V_{O1}-$Bi_2Sn_2O_{7-x}$(Sn-adjacent) and V_{O2}-$Bi_2Sn_2O_{7-x}$(Bi-adjacent): (a) real part (b) imaginary part.